

quarter (23%) of the SPCH targets are differentially expressed (table S6) and SPCH may activate or repress a large number of its targets directly.

Meristemoid-active stomatal regulators are among the direct SPCH targets (Fig. 2F, fig. S8A, fig. S9, and table S7). SPCH binds to its own promoter and to the promoter of genes that encode its heterodimeric bHLH partners, ICE1/SCRM and SCRM2 (14), and induces their expression (Fig. 2, F and G, and fig. S8A). Although initial activation of SPCH may not require SPCH protein (fig. S10), this positive feedback loop may be an essential part of a bistable switch that converts the initially low and stochastic expression of SPCH into an active SPCH-SCRM heterodimer to drive stomatal lineage fates. SPCH also binds and activates expression of genes encoding the secreted ligand EPF2, the receptor TMM, and the ERECTA family of receptor-like kinases (Fig. 2, F and G, and fig. S8A), all of which enforce proper patterning by restricting proliferation in the early stomatal lineage and act upstream of kinases that tar-

get SPCH for posttranslational down-regulation (4, 15–17). Further, SPCH binds to the promoters and activates expression of *BASL* and *POLAR*, which encode polarly localized proteins, suggesting a direct role in regulating the ACD process (Fig. 2, F and G). SPCH binding is not associated with genes that encode a later expressed stomatal lineage EPF (*EPF1*), an EPF not expressed in the stomatal lineage (*CHALLAH*) or the broadly expressed mitogen-activated protein kinase kinase kinase (MAPKKK) YODA (fig. S8B). Taken together, our ChIP-seq and RNA-seq data reveal the broad and direct roles of SPCH in sustaining a SPCH transcriptional cascade, establishing meristemoid identity and mediating ACDs.

The CDCGTG motif appears in the SPCH-bound regions of stomatal targets like *ICE1*, *TMM*, and *ERL2*. In *ICE1*, SPCH binds in two peaks centered on the locations of two CDCGTG motifs (fig. S11). To test the role of SPCH-binding motifs in *ICE1* expression, we generated a reporter bearing point mutations in the two peak-associated motifs (Fig.

2H) to compare to the WT reporter. Consistent with previous reports (14), expression of the WT promoter reporter (*ICE1pro*) was observed in the stomatal lineage; however, the mutant reporter (*mICE1pro*) was nearly undetectable (Fig. 2H and fig. S12). Similar dependence was seen with the SPCH-up-regulated gene *At2g34510*, which contains CDCGTG within a strong intronic SPCH binding peak. Deletion of the SPCH binding region abrogated early stomatal lineage-specific expression (fig. S13).

An intriguing meristemoid behavior is the ability to self-renew through ACDs. Beyond requirements for SPCH activity and the polarly localized BASL (Fig. 2F), however, little is known about the ACD process. Among SPCH targets, *ARK3/AtKINUa* (Fig. 3A) caught our attention as it encodes a plant-specific kinesin in the preprophase band (18). In plants, the preprophase band marks the future division plane (19). Confocal analysis of *ARK3pro:ARK3-YFP* showed localization to preprophase bands of asymmetrically

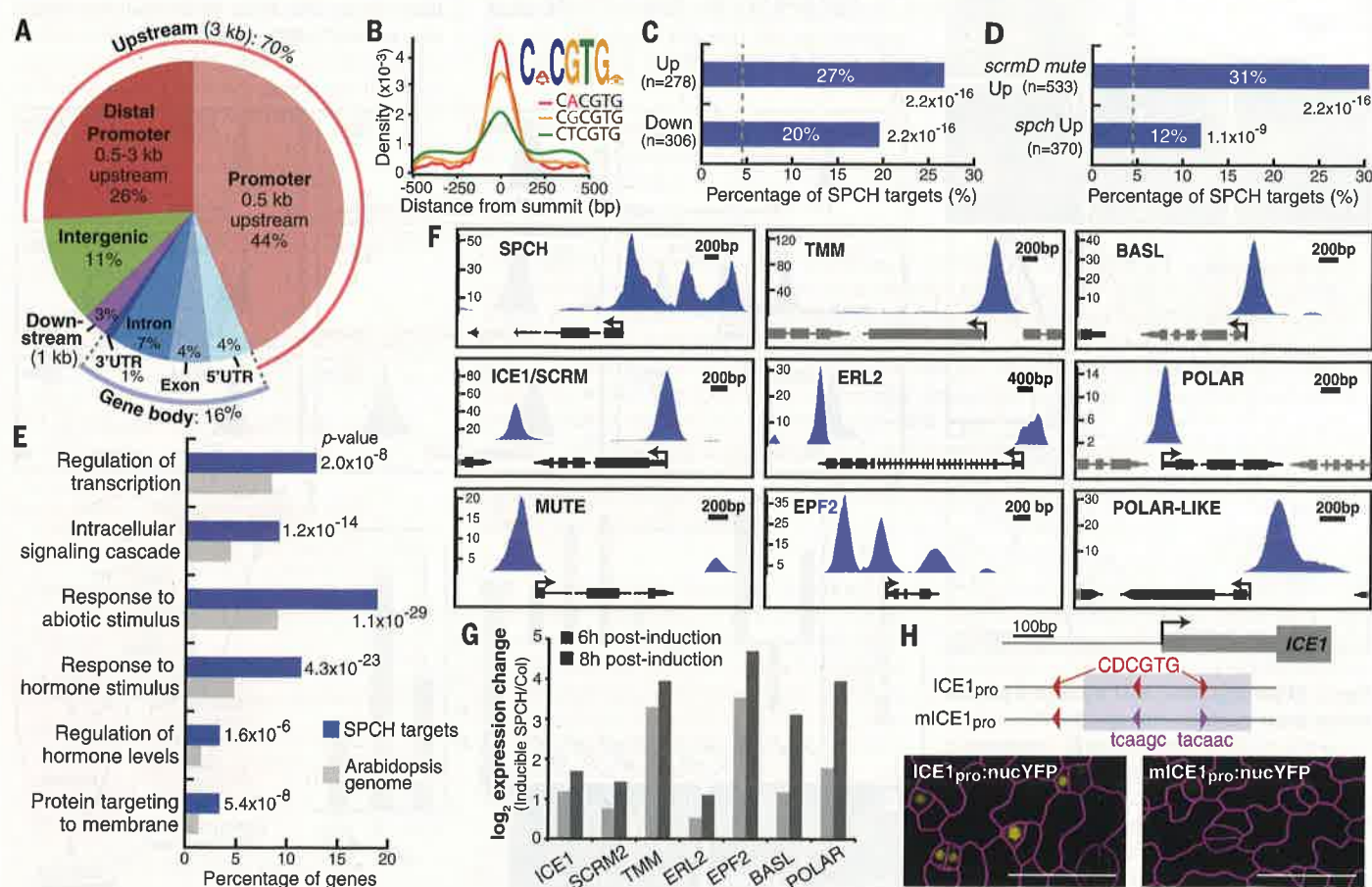


**Fig. 2. Genome-wide analysis of SPCH-binding targets reveals direct roles in lineage specification and asymmetric cell divisions.** (A) Distribution of SPCH-binding peaks relative to gene structure. (B) Top-scoring motif (E value,  $7.5 \times 10^{-365}$ ) and the position of its three variants in SPCH-binding peaks. (C and D) Percentage of SPCH targets among differentially expressed genes in RNA-seq analysis of inducible SPCH1-4A (C), and microarray analysis of meristemoid-enriched (*scrmD* mute) or -depleted (*spch*) mutants (13) (D). *P* values are calculated by Fisher's exact test. Dashed line indicates percentage by chance. (E) Select enriched GO terms of SPCH

target genes. (F and G) SPCH binds and activates key stomatal regulators. ChIP-seq profiles of select stomatal genes (F). The y axis represents peak score (CSAR), and arrows indicate gene orientation and transcriptional start sites. Gene expression changes upon induction of SPCH in RNA-seq analysis (G). (H) Importance of SPCH-binding motif (red) on *ICE1* expression. Mutation of two motifs (purple, *mICE1pro*) within the SPCH-binding peak (blue shading) abrogates *ICE1* expression (yellow). Confocal images of 4-dpg abaxial cotyledons have ML1pro:mCherry-RC12A–marked cell outlines (purple). Scale bar, 40  $\mu$ m.

from an epidermal cell lineage (Fig. 1A) (4, 5). Two populations of stomatal precursor stem cells, meristemoid mother cells and meristemoids, have limited self-renewing properties and proliferate without the benefit of a stem cell niche (4–6). These stem cells are created through the post-embryonic activity of *SPEECHLESS* (SPCH) in a subset of protodermal cells (7, 8). SPCH is a control point through which developmental, environmental, and phytohormone signals are integrated (4, 5). However, no targets of SPCH have been reported, and thus the sphere of its regulatory influence is unknown. Here, we develop a ChIP method optimized for rare developmental regulators and profile the genome-wide binding of SPCH *in vivo*. In combination with multiple transcriptional response data sets, our ChIP-sequencing (ChIP-seq) data indicate that SPCH programs an entire lineage by promoting fate transitions and asymmetric cell divisions (ACDs). SPCH also modulates the sensitivity of stomatal lineage cells to hormone and peptide/receptor-mediated signaling. Our results suggest how this lineage exhibits considerable autonomy while still coordinating with the overall organ development program.

Like many developmental regulators, SPCH expression is transient and limited to few cells (Fig. 1A). Standard ChIP assays on SPCH yielded only modest target enrichment (~4-fold, Fig. 1C, blue box), and thus we needed improved ChIP sensitivity for the detection of endogenously weak signals. We hypothesized that if background signals in a ChIP assay could be kept low, increasing the experimental scale would lead to a disproportional increase in signals from targets (true signal) over background (Fig. 1B). Therefore, performing ChIP at a large scale may achieve high target en-

richment even for low-abundance proteins. We tested this hypothesis with ChIPs at three different scales on a *spch* mutant line bearing a complementing, Myc-tagged SPCH variant driven by its native promoter (SPCHpro:SPCH2-4A-MYC) (fig. S1). The scales represented 4, 8, and 16 times (or 6, 12, and 24 g) the input materials used in a typical *Arabidopsis* ChIP experiment. ChIP-qPCR (quantitative polymerase chain reaction) assays of SPCH on the promoter of *TOO MANY MOUTHS* (*TMM*) showed that scale increase improves target enrichment up to 600-fold at 16x (or a >30-fold increase in enrichment with a 4-fold scale increase) (Fig. 1C, three rightmost columns). Thus, weak signals can be enhanced by maximizing input. We termed this method Maximized Objects for Better Enrichment (MOBE)-ChIP.

To profile genome-wide binding events of SPCH, we performed and pooled six MOBE-ChIPs on SPCHpro:SPCH2-4A-MYC and on a wild-type (WT) control for high-throughput sequencing (scale, 16x; total, 144 grams per genotype) (Fig. 1C, red box, and fig. S2B). For comparison, standard ChIP-seq was also included [pooled from nine independent ChIPs on SPCHpro:SPCH2-4A-YFP (yellow fluorescent protein) and nucGFP (green fluorescent protein) at 4x] (Fig. 1C, blue box, and fig. S2A). MOBE-ChIP-seq confirmed the ChIP-qPCR results at the *TMM* promoter, revealing a single peak with an enrichment score of 178 [ $-\log_{10}(q\text{ value})$ ,  $1.2 \times 10^6$ ]; the corresponding peak from our 4x run had a score of 1.2 [ $-\log_{10}(q\text{ value})$ , 5.7] (Fig. 1D). Low background signal is also a genome-wide trend. Using the peak-calling algorithm ChIP-seq Analysis in R (CSAR) (9), we detected peaks with an enrichment score as low as 1.62 at a false discovery rate (FDR) of  $1 \times 10^{-6}$ , in contrast to other studies whose peaks above threshold scores of 1.85 and 79.6 were detected at FDRs of 0.01 and 0.001, respectively (table S1) (10, 11). The ability to identify these low-coverage peaks is indicative of the power of signal enrichment. Thus, through MOBE-ChIP-seq, we generated a comprehensive *in vivo* genome-wide binding map of SPCH.

Using two complementary peak-calling pipelines, we identified 8327 SPCH-bound regions (tables S2 and S3). Seventy percent of the SPCH binding peaks are associated with gene promoters, mostly within 500 base pairs upstream of the transcriptional start site (Fig. 2A and fig. S3). De novo discovery of enriched motifs in the binding peaks identified CDCGTG as the top-scoring motif; this variant of the E-box (CACGTG), to which basic helix-loop-helix (bHLH) proteins typically bind, is enriched at the summit of the SPCH peaks (Fig. 2B and fig. S4).

To focus on loci most likely to respond transcriptionally to SPCH binding, we generated a “high-confidence” subset of peaks that were non-intergenic with enrichment scores  $\geq 10$  (table S2). Among the high-confidence targets, Gene Ontology (GO) terms for genes involved in regulation of transcription, signaling, response to stimulus, and regulation of hormone levels were significantly enriched (Fig. 2E, fig. S5, and table S4). This suggests that in the initiation of the stomatal lineage, SPCH could act as a mediator of environmental and hormone inputs that are translated into further downstream transcriptional and signaling networks. The enrichment of the GO term “protein targeting to membrane” is interesting given the membrane-associated polarization of stomatal lineage proteins BASL and POLAR during asymmetric divisions (12, 13).

To correlate SPCH binding with transcriptional responses on a genome-wide scale, we compared the high-confidence SPCH targets to data sets representing genes expressed in response to SPCH induction (fig. S6 and table S5) and those enriched for genes preferentially expressed in the stomatal lineage (13) (fig. S7). Significant enrichment of the SPCH targets was found among genes both up- and down-regulated in response to SPCH induction (27 and 20%, respectively) (Fig. 2C) and in plants with excess or no meristemoids (31 and 12%) (Fig. 2D). By chance, SPCH would be predicted to bind to ~4.5% of genes in the data sets (1517 targets out of 33,602 *Arabidopsis* genes). Overall, these comparisons indicate that nearly a

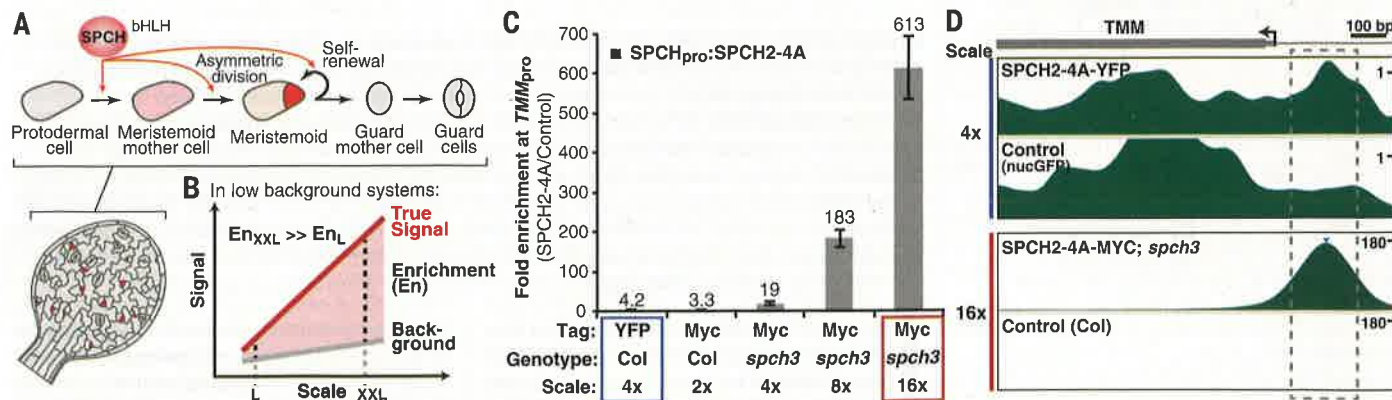


**Fig. 1. Chromatin immunoprecipitation (ChIP) optimized for cell-type-specific studies in vivo.** (A) *Arabidopsis* stomatal development scheme. SPCH controls the initiation and proliferation of the stem cell-like stomatal lineage precursors (pink and red cells). (B) Model for improving target enrichment in ChIPs through increasing experimental scale. (C and D) ChIPs at larger scales improve target enrichments. ChIP-qPCR assays of a SPCH variant on the *TMM* promoter performed at the indicated conditions (C). SPCH ChIP-seq profiles at *TMM* (D) generated from ChIPs at 4x and 16x [blue and red box in (C), respectively]. The y axis represents the enrichment values; note scales. Dashed box marks the SPCH-binding region.



dividing meristemoids (Fig. 3B). Coexpression with SPCHpro:SPCH-CFP indicated that SPCH precedes ARK3, consistent with SPCH activating ARK3 expression (Fig. 3, C to E). To ascertain its function in the stomatal lineage, we reduced ARK3 expression by driving an artificial microRNA against it with the SPCH promoter (*SPCHpro:amiR-ark3*). In the cotyledon epidermis of *amiR-ark3*-expressing plants, we observed clusters of meristemoid-like small cells at 4 days postgermination (dpg) that developed into clusters of stomata at 11 days (Fig. 3, G and I, brackets). These small cell clusters, which displayed diminished physical asymmetry, appear to arise from misplaced but complete division planes. Notably, cell wall stubs or other evidence of incomplete divisions were not observed. The *amiR-ark3* phenotypes resembled those associated with *basl* mutants (12) and are hallmarks of loss of ACD capacity. Thus, ARK3

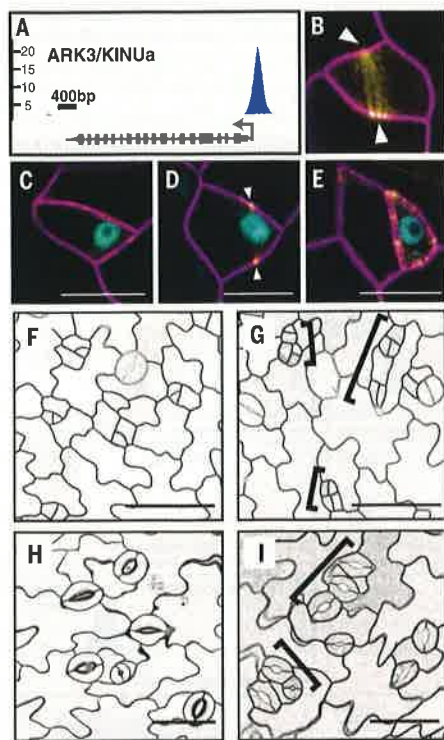


**Fig. 3. SPCH regulates ACD through a preprophase band-localized kinesin.** (A) SPCH ChIP-seq profile of *ARK3/KINUA*. (B to E) Expression of *ARK3pro:ARK3-YFP* (yellow) (B) and its coexpression with *SPCHpro:SPCH-CFP* (blue) [(C) to (E)] before (C), during (B) and (D), and after (E) a stomatal ACD. Arrowheads indicate the preprophase band. (F to I) ACD defects in *SPCHpro:amiR-ark3* [(G) and (I)], compared with Col [(F) and (H)]. Brackets mark clusters of small cells (G) or guard cells (I). Confocal images are of 3- [(B) to (E)], 4- [(F) and (G)] and 11-day [(H) and (I)] abaxial cotyledons with *ML1pro:mCherry-RC12A*-marked cell outlines. To display the cells in (E) in the same orientation as panels (C) and (D), we rotated the image in (E) and filled in the nonimaged space in the upper right corner with a black triangle (dashed line). Scale bars, 10  $\mu$ m [(C) to (E)], 50  $\mu$ m [(F) to (I)].

appears to be a new player essential for ACD, possibly through regulating preprophase band placement, and establishes a direct link between SPCH and the ACD machinery.

SPCH initiates a lineage with autonomous control over cell division and fate determination. Nonetheless, the stomatal lineage is also coordinated with developmental programs operating across tissues and organs. Phytohormones play critical roles in coordinating development, and recent reports indicate that auxin, brassinosteroid (BR), and abscisic acid regulate stomatal development (20–23). BR controls stomatal development through phosphorylation of YODA and SPCH by its central glycogen synthase kinase 3-like kinase, BIN2 (Fig. 4F) (21, 22). Among SPCH target categories, BR biosynthetic and response genes show significant enrichment (fig. S14). Notably, SPCH binds to the promoters of *BIN2* and *CPD*, which encodes an essential enzyme for BR biosynthesis (Fig. 4, A and F), and the absence of *CPD* results in stomatal overproduction (24). We tested the effect of SPCH on the expression of BR genes by reverse transcription qPCR (RT-qPCR) in the meristemoid-enriched line *SPCHpro:SPCH2-4A-YFP* (Fig. 4B).

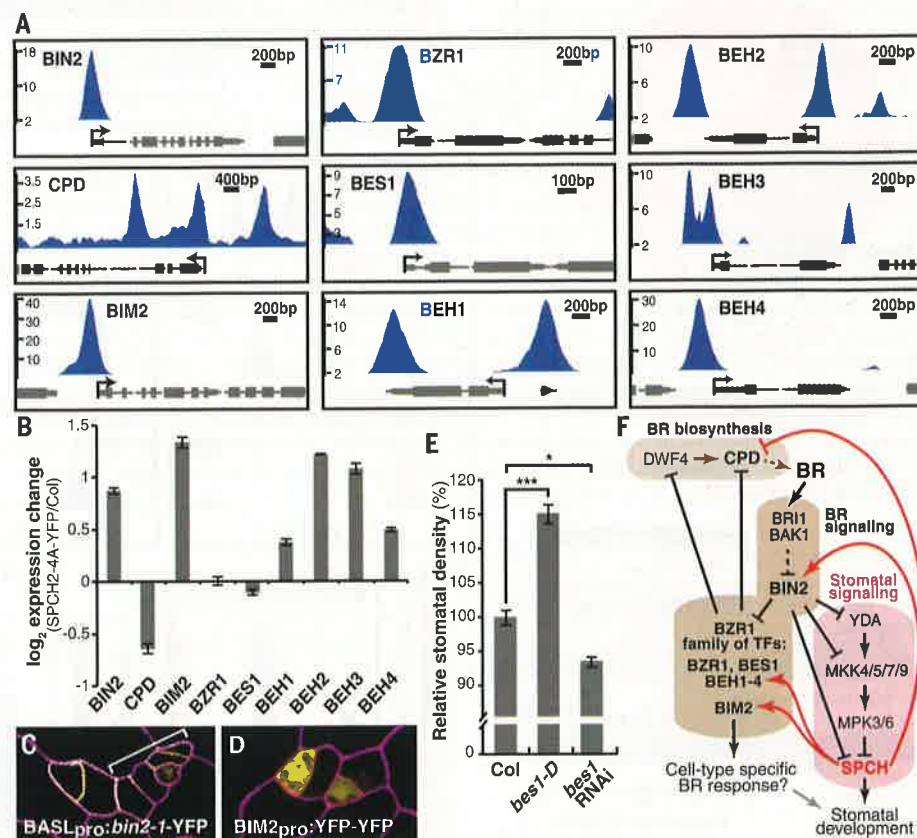


**Fig. 4. Feedback regulation of brassinosteroid biosynthesis and signaling by SPCH.** (A) ChIP-seq profiles of select brassinosteroid (BR) pathway genes (labeled as in Fig. 2F). (B) RT-qPCR analysis of BR genes in 4-dpg *SPCHpro:SPCH2-4A-YFP* and Col seedlings. Values are means  $\pm$  SEM. (C and D) Confocal images of 3-dpg adaxial cotyledons with propidium iodide-stained cell outlines (purple). Stomatal lineage-specific expression of hyperactive *BIN2* (yellow) induces lineage proliferation (bracket) (C). Stomatal lineage expression pattern of *BIM2pro:YFP-YFP* (yellow) (D). (E) Alteration of stomatal density in gain-of-function *BES1pro:bes1-D* and *bes1-RNAi* knockdown. \* $P < 0.05$ , \*\*\* $P < 0.001$  (Wilcoxon rank sum test). (F) Model of SPCH-BR pathway interactions. SPCH, a target of BR signaling, feeds back (positively, red arrows, or negatively, red T-bar) upon transcription of multiple pathway members.

Consistent with inhibition of BR signaling, we found that *BIN2* expression is elevated, whereas *CPD* is repressed (Fig. 4B). Supporting *BIN2*'s role in promoting SPCH function, stomatal lineage-specific expression of *BIN2-1* led to small cell clusters in cotyledons, similar to those observed upon SPCH overexpression (Fig. 4C). Thus, our results suggest the presence of feedback by SPCH counteracting BR signaling (Fig. 4F). SPCH also binds to genes encoding the BR signaling effectors, the BZR1 family of transcription factors (BZR1, BES1/BZR2, and BEH1 to BEH4), and BIM2, the putative dimeric partner of BES1 (25–27). *BEH1* to *BEH4* and *BIM2* were up-regulated in the meristemoid-enriched mutant, and *BIM2* exhibited stomatal lineage-specific expression (Fig. 4, B and D). Epidermal expression of *bes1-D* (26) correlates with an increase in stomatal density, whereas a *bes1* RNA interference (RNAi) knockdown line (27) exhibited a trend toward lower stomatal density (Fig. 4E). This role in promoting stomatal development may be explained through the known repression of the BR biosynthetic genes by the BZR1 family (28). Thus, SPCH-mediated induction of *BIN2* and repression of *CPD* (either

two-photon uncaging. For optogenetic stimulation of dopaminergic fibers, a Cre-dependent adeno-associated virus (AAV) vector expressing channelrhodopsin-2 (ChR2) was injected into the ventral tegmental area (VTA) of DAT-Cre mice

expressing Cre specific to dopaminergic neurons (Fig. 1A and fig. S1). The direct pathway-constituting MSNs, which mainly express dopamine 1 receptors (D1Rs) (13), were labeled by an AAV vector with a specific promoter for D1R-MSNs (Fig. 1A

and fig. S1). In acute coronal slices, including the nucleus accumbens (NAc) core, whole-cell recordings were obtained from the identified D1R-MSNs. Dendritic spines were visualized by means of two-photon microscopy (980 nm) detecting

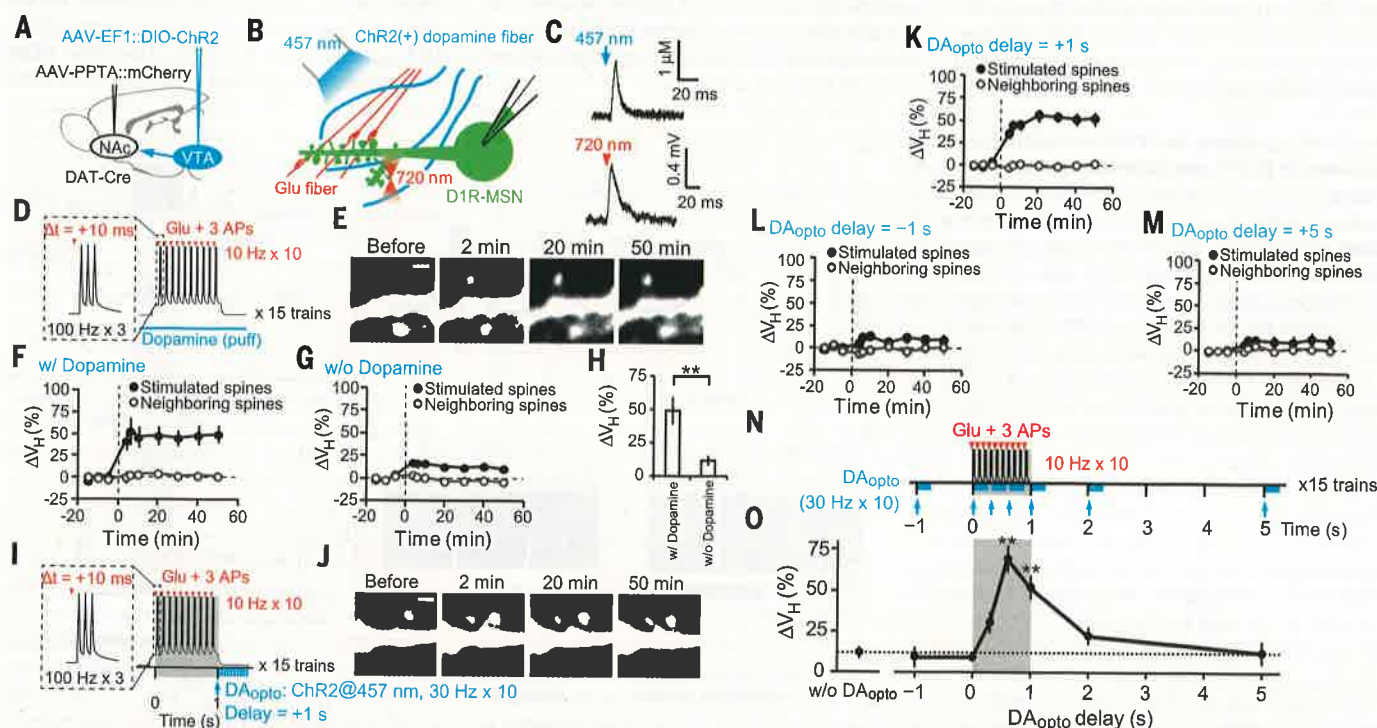
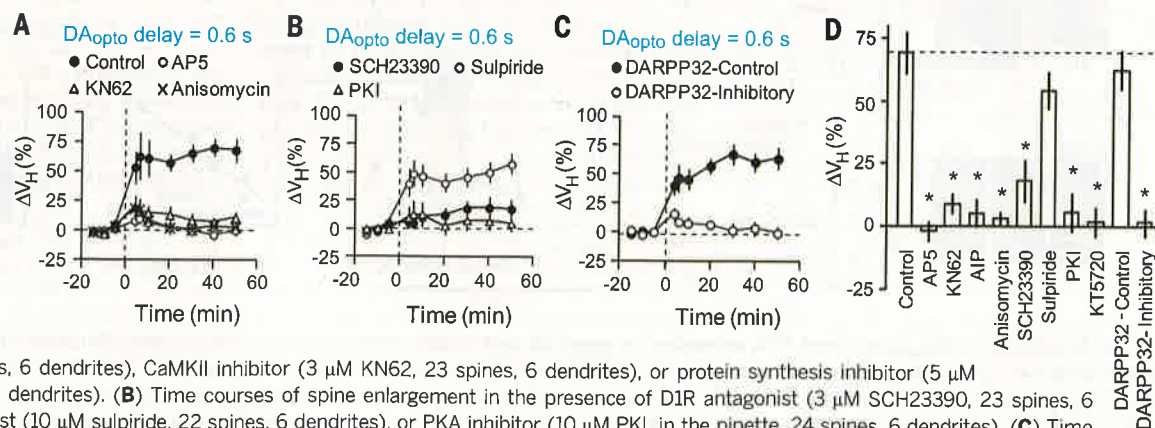


**Fig. 1. A temporal profile of dopamine actions on spine enlargement.** (A) Injection of AAV vectors for ChR2 and the D1R-MSN marker (PPTA-mCherry) in 3-week-old DAT-Cre mice. (B) Selective stimulation of dopaminergic and glutamatergic inputs by means of blue laser field irradiation to ChR2 and two-photon uncaging of caged-glutamate at a single spine, respectively, in acute slices of NAc obtained from 5- to 7-week-old mice. (C) An amperometric measurement of dopamine (top) by carbon-fiber electrode and whole-cell recording of glutamate-induced current (bottom, 2pEPSP) in identified D1R-MSNs. (D) An STDP protocol with dopamine puff application. (E) Images of the dendritic spine (red arrowhead) that received STDP stimulation in the presence of dopamine (100  $\mu$ M). (F and G) Time courses of spine enlargement in the presence [(F), 13 spines, 4 dendrites] and absence of

dopamine [(G), 58 spines, 14 dendrites]. (H) Amplitudes of spine enlargements with or without dopamine.  $**P = 0.0041$  by Mann-Whitney U test. (I) STDP with repetitive activation of dopaminergic fibers containing ChR2 (blue lines) at 30 Hz, 10 times ( $DA_{opto}$ ). (J) Images of the dendritic spine (arrowhead) that received STDP +  $DA_{opto}$  with a delay of 1 s. (K to M) Time courses of spine enlargement induced by STDP +  $DA_{opto}$  at 1 s [(K), 48 spines, 14 dendrites], -1 s [(L), 20 spines, 5 dendrites] and 5 s [(M), 28 spines, 7 dendrites] after STDP onset. (N) Timings of  $DA_{opto}$  application. (O) Increases in spine volumes by STDP +  $DA_{opto}$  plotted versus  $DA_{opto}$  delay (fig. S2, A to C). Data are presented as mean  $\pm$  SEM.  $P = 4.2 \times 10^{-6}$  with Kruskal-Wallis and  $**P = 0.0018$  (0.6 s) and 0.0027 (1 s) by Steel test in comparison with STDP in the absence of  $DA_{opto}$ . Scale bars, 1  $\mu$ m.

**Fig. 2. Pharmacology of spine enlargement induced by STDP plus  $DA_{opto}$  with a 0.6-s delay.**



(50  $\mu$ M D-AP5, 22 spines, 6 dendrites), CaMKII inhibitor (3  $\mu$ M KN62, 23 spines, 6 dendrites), or protein synthesis inhibitor (5  $\mu$ M anisomycin, 25 spines, 6 dendrites). (B) Time courses of spine enlargement in the presence of D1R antagonist (3  $\mu$ M SCH23390, 23 spines, 6 dendrites), D2R antagonist (10  $\mu$ M sulpiride, 22 spines, 6 dendrites), or PKA inhibitor (10  $\mu$ M PKI, in the pipette, 24 spines, 6 dendrites). (C) Time courses of spine enlargement in the presence of inhibitory (100  $\mu$ M, in the pipette, 24 spines, 6 dendrites) or control peptide for DARPP-32 (100  $\mu$ M, in the pipette, 24 spines, 6 dendrites). (D) Averaged volume changes in the absence and presence of the compounds. Data are presented as mean  $\pm$  SEM.  $P = 3.4 \times 10^{-6}$  with Kruskal-Wallis and  $*P = 0.023$  (AP5), 0.023 (KN62), 0.037 (AIP) (fig. S5A), 0.023 (anisolomycin), 0.035 (SCH23390), 0.023 (PKI), 0.037 (KT5720) (fig. S5A), and 0.023 (DARPP-32 inhibitory peptide) with Steel test.



**Fig. 1. Clinical phenotype and pedigree of the patients.** (A) Top: Computed tomography images of lung and brain from patient A.II.1. Bottom: Histological section (magnification 20 $\times$ ) from a duodenal biopsy from a healthy donor (HD) and patient A.II.1 stained for CD3 (brown cells), showing an increased number of transepithelial T cells within the villi. (B) Flow cytometric analyses of CD4 $^{+}$  cells or total lymphocytes stained for the indicated surface markers from a healthy donor and patient A.II.1. Data showing decreased CD45RA $^{+}$ CD62L $^{+}$  naïve CD4 $^{+}$  T cells are representative of three patients (A.I.1, A.II.1, and B.I.1). Programmed cell death-1 (PD1) expression data shown are representative of five patients (A.I.1, A.II.1, B.I.1, C.II.1, and D.II.1) and three healthy donors. Data showing decreased circulating B cells are representative of two patients (A.I.1 and A.II.1). (C) Mutations in patient alleles displayed on a schematic of the four exons of *CTLA4*, pedigrees, and phenotype summary highlighting organs (gray) with inflammatory infiltrates and autoimmune cytopenias for affected family members. TM, transmembrane domain. (D) Protein and mRNA expression of CTLA-4 in T<sub>reg</sub> cells. Left: Levels of CTLA-4 expression in T<sub>reg</sub> cells (CD4 $^{+}$ CD25 $^{+}$ FoxP3 $^{+}$ ) were assessed by intracellular staining. The numbers in the upper right corner depict mean fluorescence intensity (MFI) of anti-CD152 (CTLA-4) staining. Dotted line indicates the peak of CTLA-4 expression in a healthy donor. Data shown are representative of three experiments. Right: Levels of *CTLA4* mRNA in T<sub>reg</sub> cells (CD4 $^{+}$ CD25 $^{+}$ CD127 $^{lo}$ ) sorted from seven different healthy donors and four patients were measured by real-time PCR using the probe for *CTLA4* transcript variant 1 (full length) and normalized to GAPDH. Data are means of replicates from six experiments. For relative gene expression, all data were normalized to the same HD. The horizontal lines indicate mean values from healthy donors or patients.

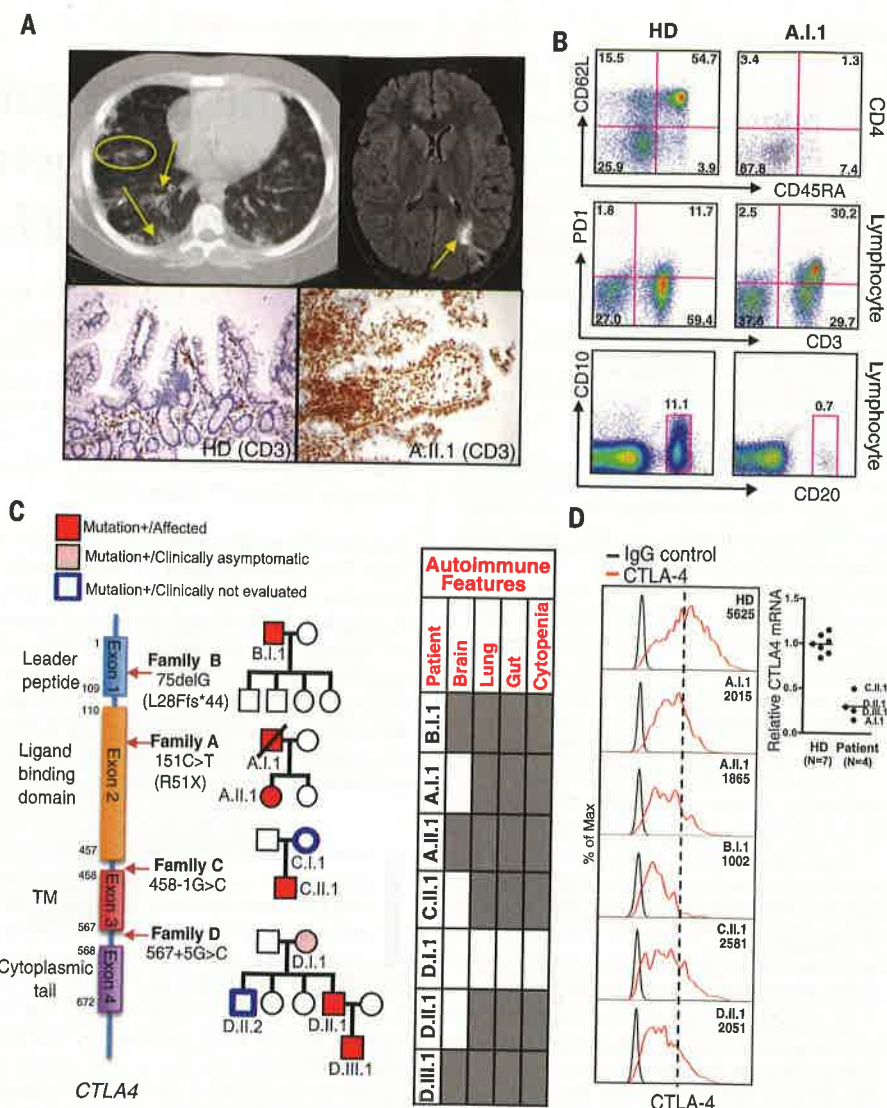


**Fig. 2. Abnormal T<sub>reg</sub> cell phenotype and function in patients.** (A) Flow cytometric analysis of FoxP3 and CD25 in CD4 $^{+}$  T cells from healthy donor (HD) and patients. (B) Mean fluorescence intensity of FoxP3 and CD25 in CD4 $^{+}$  FoxP3 $^{+}$  T cells from healthy donors and patients. Data are means  $\pm$  SEM of replicates of indicated patient [A.I.1 (N = 7), A.II.1 (N = 1), B.I.1 (N = 2), C.II.1 (N = 2), D.II.1 (N = 4)] and 10 healthy donors. The N values represent number of replicates from each patient. \*\*\*P = 0.0007 (Mann-Whitney test). Bar graph: Percentage of CD25 $^{+}$  and CD25 $^{-}$  cells among CD4 $^{+}$ FoxP3 $^{+}$  in 10 healthy donors and five patients. (C) Autologous and heterologous suppressive activities of T<sub>reg</sub> cells from five healthy donors and four patients (A.I.1, B.I.1, C.II.1, and D.II.1). The horizontal lines indicate the mean values. Data are from three experiments, with each indicated patient paired with one or two healthy donors. \*P = 0.0239, \*\*P = 0.0037 (paired t test).

